Oblique stripe solutions of channel flow

Chaitanya S. Paranjape[1,†], **Yohann Duguet**[2] **and Björn Hof**[1]

[1]Nonlinear Dynamics and Turbulence Group, IST Austria, 3400 Klosterneuburg, Austria

[2]LIMSI-CNRS, Campus Universitaire d'Orsay, Université Paris-Saclay, 91405 Orsay, France

With decreasing Reynolds number, *Re*, turbulence in channel flow becomes spatio-temporally intermittent and self-organises into solitary stripes oblique to the mean flow direction. We report here the existence of localised nonlinear travelling wave solutions of the Navier–Stokes equations possessing this obliqueness property. Such solutions are identified numerically using edge tracking coupled with arclength continuation. All solutions emerge in saddle-node bifurcations at values of *Re* lower than the non-localised solutions. Relative periodic orbit solutions bifurcating from branches of travelling waves have also been computed. A complete parametric study is performed, including their stability, the investigation of their large-scale flow, and the robustness to changes of the numerical domain.

Key words: bifurcation, transition to turbulence

1. Introduction

The study of the transition to turbulence usually starts with the investigation of the linear instabilities of the laminar solution. Plane Poiseuille flow (PPf), the solution of channel flow with a parabolic profile, is one of the few analytical solutions of the Navier–Stokes equations. Its stability has been studied extensively, with the ambition to predict the transition to turbulence in this simple flow geometry. This solution loses its stability in favour of two-dimensional Tollmien–Schlichting (TS) waves at $Re = 5772$, where the Reynolds number $Re = U_{cl}h/\nu$ is based on U_{cl} – the centreline velocity of the corresponding Poiseuille flow solution, h – the half-gap, and ν – the kinematic viscosity of the fluid (Orszag 1971). Turbulence, however, is already found in channel experiments at $Re = 1000$ and below. Although the TS instability is subcritical in *Re*, (Stuart 1960; Ehrenstein & Koch 1991) the bifurcated branches fail to reach the low values of *Re* where the onset of turbulence is reported in early transition experiments (Carlson, Widnall & Peeters 1982; Nishioka & Asai 1985; Alavyoon, Henningson & Alfredsson 1986; Klingmann 1992; Seki & Matsubara 2012; Lemoult, Aider & Wesfreid 2013). More critically, the TS waves,

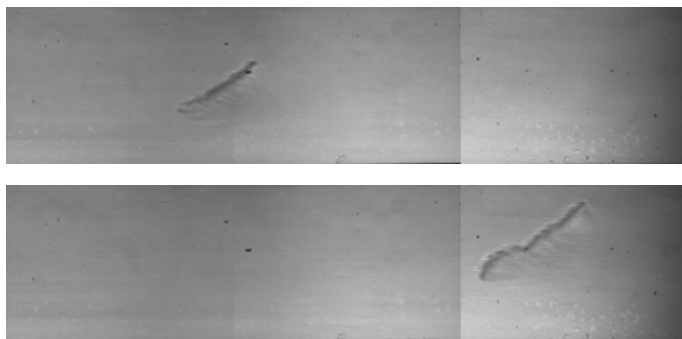† Email address for correspondence: cparanjape@ist.ac.at

FIGURE 1. Experimental observation of an elongating isolated oblique stripe at $Re = 700$ in a water channel as it travels downstream. The flow is from the left to the right. Reflective mica particles were added for visualisation.

having only spanwise vorticity, bear little structural resemblance with the coherent structures observed in the corresponding turbulent regimes, which are characterised by quasi-streamwise streaks and vortices.

From the analysis of the self-sustaining process of turbulence (Hamilton, Kim & Waleffe 1995), it has become clear that different solutions of the governing Navier–Stokes equations ought to exist, which capture key components of turbulent flows and are more relevant to the transition process (Jiménez *et al.* 2005; Kawahara, Uhlmann & Van Veen 2012). The first solutions were identified as steady states in plane Couette flow by Nagata (1990), followed by many others (see e.g. Gibson, Halcrow & Cvitanović (2009)). Many solutions have been found in other shear flow geometries in the form of travelling waves (TWs), see Waleffe (2001), Nagata & Deguchi (2013), Park & Graham (2015), Neelavara, Duguet & Lusseyran (2017), Wall & Nagata (2016) in the context of channel flow and Faisst & Eckhardt (2003), Wedin & Kerswell (2004) for pipe flow. They are disconnected from the laminar profile and all are linearly unstable. The entanglement of their stable and unstable manifolds has been conjectured to form a deterministic backbone for the low-Re turbulent dynamics (Kawahara *et al.* 2012). Many of these studies were performed in small periodic domains. Though conceptually useful, these studies are motivated by higher Re wall turbulence studies (Jiménez & Moin 1991) and turn out to be inadequate to capture crucial characteristics of lower Re turbulent flows, such as spatial localisation. Indeed, ample experimental and numerical evidence from studies in large domains show that wall-bounded turbulence at the lowest possible values of Re remains localised. Besides, the corresponding laminar–turbulent interfaces display non-zero angles with respect to the laminar flow direction (Coles 1965; Prigent *et al.* 2002; Tsukahara *et al.* 2005; Hashimoto *et al.* 2009; Duguet, Schlatter & Henningson 2010; Fukudome & Iida 2012; Xiong *et al.* 2015). Starting from fully turbulent flow, as Re is decreased, criss-cross stripe patterns appear. As Re is decreased further, the mean spacing between these stripes of turbulence increases, to the extent that they appear isolated in an otherwise laminar environment (see Tsukahara & Ishida (2015), Tao, Eckhardt & Xiong (2018), Paranjape (2019)). An experimental realisation of a stripe in channel flow is shown in figure 1. Oblique stripes are common to many wall-bounded shear flows at the onset (in Re) of turbulence (Tuckerman, Chantry & Barkley 2019). These include the cases, in historical order, of Taylor–Couette flow (Coles 1965), plane Couette flow (Prigent *et al.* 2002), rotor-stator flow (Cros & Le

Gal 2002) and annular pipes (Ishida, Duguet & Tsukahara 2016, 2017; Kunii *et al.* 2019).

The appropriate bifurcation scenario rationalising the appearance and self-sustenance of such oblique turbulent structures has not been clarified yet. We expect it to start from a branch of nonlinear solutions of the Navier–Stokes equations possessing the following properties: (a) spatial localisation, (b) an oblique orientation with respect to the mean flow, with angles comparable to experimental observations, (c) quasi-streamwise vortices and streaks not aligned with the interface. In the present study, we demonstrate numerically the existence of nonlinear TWs satisfying all the above properties at once. These TWs form a large family of nonlinear states parametrised by two wavelengths and by their angle with respect to the streamwise direction. Their computation is a necessary step towards an improved mathematical understanding of subcritical transition directly from the governing Navier–Stokes equations.

The paper is structured as follows: the numerical methodology is explained in § 2 and a parametric study of the TWs is detailed in § 3. Eventually, all these numerical results, and their relevance to the experimentally observed transition phenomenon, are discussed in § 4.

2. Numerical aspects

The approach used throughout this study is based on the numerical code Channelflow (Gibson 2014), which integrates the incompressible Navier–Stokes equations in time in a parallelepipedic geometry. When non-dimensionalised using the centreline velocity U_{cl} of the laminar flow at the equivalent flow rate, the half-gap h and the kinematic viscosity ν, the Navier–Stokes equations for the velocity–pressure perturbation $(\boldsymbol{u}, p)$ to the base flow $(\boldsymbol{U}_L, P)$ take the following form

$$\frac{\partial \boldsymbol{u}}{\partial t} + (\boldsymbol{u} \cdot \boldsymbol{\nabla})\boldsymbol{u} + (\boldsymbol{u} \cdot \boldsymbol{\nabla})\boldsymbol{U}_L + (\boldsymbol{U}_L \cdot \boldsymbol{\nabla})\boldsymbol{u} = -\boldsymbol{\nabla}p + \frac{1}{Re}\nabla^2\boldsymbol{u} + \boldsymbol{f}(t)\boldsymbol{\nabla} \cdot \boldsymbol{u} = 0, \quad (2.1)$$

where $Re = U_{cl}h/\nu$. $\boldsymbol{U}_L$ is the streamwise base flow, $\boldsymbol{f}(t)$ is a time-dependent forcing term mimicking an imposed streamwise pressure gradient. The flow rate in both planar directions x and z is held constant by adapting the amplitude of the forcing term $\boldsymbol{f}(t)$ at every time step. No-slip boundary conditions are imposed at the walls of the channel $(y = \pm 1)$, resulting in

$$\boldsymbol{u}(x, \pm 1, z) = 0. \quad (2.2)$$

The spectral decomposition of the velocity field reads

$$\boldsymbol{u} = \sum_{k,m,n} T_n(y)\mathrm{e}^{\mathrm{i}(k\alpha x + m\beta z)}, \quad (2.3)$$

where $T_n(y)$ are Chebyshev polynomials, and $(\alpha = 2\pi/L_x,\ \beta = 2\pi/L_z)$ is the fundamental wave vector, where L_x and L_z are lengths of the rectangular domain in planar directions x and z. The summation extends from $k = N_x/2 + 1$ to $N_x/2$, from $m = N_z/2 + 1$ to $N_z/2$, and from $n = 0$ to $N_y - 1$, where N_x, N_y and N_z are integers. The use of Fourier modes in (2.3) implies periodicity in the planar directions x and z. The time-stepping algorithm with variable time step combines a Crank–Nicolson scheme with a second order Adams–Bashforth scheme for the nonlinear terms, and the maximum time step is fixed to 0.0325 in units of h/U_{cl}. By convention, N_x and N_z are understood here as the number of modes before dealiasing.
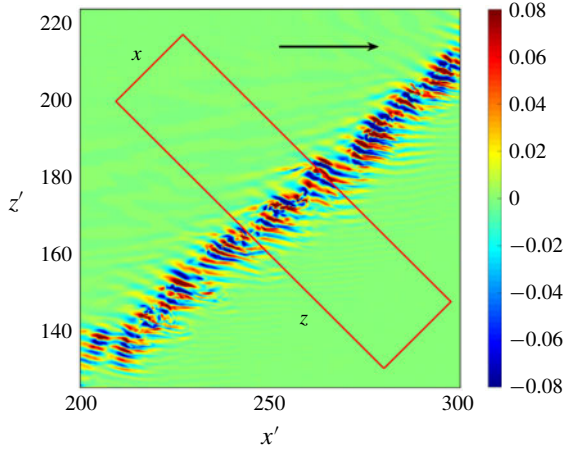
FIGURE 2. Direct numerical simulation of a sustained turbulent stripe in a large domain with $L_{x'} = L_{z'} = 400$, no tilting (flow from bottom to top). Isocontours of wall-normal velocity $v(x, y = 0, z)$ for $Re = 660$. The oblique red rectangle illustrates the concept of tilted domain (Barkley & Tuckerman 2005) with periodic boundary conditions in x and z. By construction, the shorter side of the domain is parallel to the stripe.

A tilted domain, as in Barkley & Tuckerman (2005, 2007), Tuckerman *et al.* (2014), is used in order to capture solutions in the form of oblique stripes. If x', y and z' denote the usual streamwise, wall-normal and spanwise coordinates, and $\boldsymbol{e}_{x'}$, $\boldsymbol{e}_y$, $\boldsymbol{e}_{z'}$ are the corresponding unit vectors, we define here the directions x and z associated with the new unit vectors $\boldsymbol{e}_x$ and $\boldsymbol{e}_z$ by

$$\boldsymbol{e}_x = \cos\theta\boldsymbol{e}_{x'} + \sin\theta\boldsymbol{e}_{z'}, \quad \boldsymbol{e}_z = \sin\theta\boldsymbol{e}_{x'} - \cos\theta\boldsymbol{e}_{z'}, \quad (2.4a,b)$$

where $0° \leqslant \theta \leqslant 90°$. These notations are consistent with Barkley & Tuckerman (2007) and Tuckerman *et al.* (2014). If $L_x \ll L_z$ and $L_x = O(h)$, then, provided there is a laminar–turbulent interface in the flow wider than $O(h)$, this interface can only be parallel to the short direction $\boldsymbol{e}_x$. The quantity θ can be thus interpreted as the angle between the physical streamwise direction and the stripe (Tuckerman *et al.* 2014). Note that no extra discrete symmetry has been imposed in any of the simulations. The concept of tilted domain is demonstrated in figure 2. There, the simulation in a larger domain is performed inside a non-tilted domain ($\theta = 0°$) of size $L_{x'} = L_{z'} = 400$ with resolution $(N_x, N_y, N_z) = (1536, 64, 1536)$.

The resolution used for a numerical domain with $(L_x, L_z) = (10, 40)$ is $N_x = 72$, $N_y = 49$ and $N_z = 256$ for all values of Re and θ reported. This is comparable with the resolution in Tuckerman *et al.* (2014) for the turbulent regimes, known to be computationally more demanding in terms of resolution than edge regimes for equivalent parameters. One can also define a local resolution ($n_x = N_x/L_x$, $n_z = N_z/L_z$) maintained in case of changes in domain size (such as in § 3.1). The current value of N_y ensures that, for values of Re sufficiently below 1000, all transverse scales are properly resolved.

In what follows, we keep primed notations (x', z', u', w') for non-tilted planar variables and non-primed notations (x, z, u, w) for planar quantities defined within a tilted domain. The physical streamwise velocity perturbation is hence denoted u' (respectively, w' for the spanwise component), while the velocity components parallel and orthogonal to the stripes are denoted u and w, respectively.

2.1. *Tools for identification of nonlinear solutions*

The observable E_v, based on the deviation from the base flow, is the wall-normal energy defined as

$$E_v = \frac{1}{2} \int_0^{L_x} \int_0^{L_z} \int_{-1}^{1} v^2 \, dx \, dy \, dz, \tag{2.5}$$

where v is the wall-normal velocity component. The total perturbation kinetic energy E is defined in a similar way with v^2 replaced by the squared norm of the disturbance velocity $|\boldsymbol{u}|^2$ (both independent of the tilting of the domain). The z-dependent energy $e(z)$ is defined by

$$e(z) = \frac{1}{2} \int_0^{L_x} \int_{-1}^{1} |\boldsymbol{u}|^2 \, dy \, dx, \tag{2.6}$$

and is such that $E = \int_0^{L_z} e(z) \, dz$. Its wall-normal counterpart $e_v(z)$ is also defined in the same manner by considering only v^2 as integrand.

Edge states are computed using the standard bisection algorithm (Skufca, Yorke & Eckhardt 2006; Schneider, Eckhardt & Yorke 2007; Duguet, Schlatter & Henningson 2009): the amplitude of an arbitrary initial condition is rescaled recursively until the flow reaches neither laminar nor turbulent level for sufficiently long observation times. The two criteria, according to which trajectories are labelled as relaminarising or transitioning, are based on threshold values for the wall-normal energy E_v (see (2.5)), both chosen after trial and error. Once machine precision is reached, the rescaling process is re-started from a state at a later time.

Several types of exact coherent states are identified during this study. In particular, TW solutions are defined by

$$\boldsymbol{u}(x, y, z, t) = \boldsymbol{u}(x + c_x T, y, z + c_z T, t + T), \tag{2.7}$$

for all t and T, where t is time and T is time period, while relative periodic orbits (RPOs) are defined as

$$\boldsymbol{u}(x, y, z, t) = \boldsymbol{u}(x + \sigma_x, y, z + \sigma_z, t + T), \tag{2.8}$$

for all t but for given values of T, σ_x and σ_z, where σ_x and σ_z are shifts in the x and z directions respectively. The Newton–Krylov algorithm included in channelflow.org, augmented by the hook–step globalisation technique (Viswanath 2007), is used to successfully converge TW solutions and RPOs with an accuracy of $O(10^{-14})$. Arclength continuation is used to track the converged states as functions of various parameters, such as Re, L_x or θ. For each converged state, application of the matrix-free Arnoldi algorithm is used to determine eigenvalues or Floquet exponents of converged solutions.

The governing system of equations, independent of the numerical domain, is equivariant with respect to the two discrete symmetries

$$S_y : [u', v, w'](x', y, z') \rightarrow [u', -v, w'](x', -y, z'), \tag{2.9}$$

$$S_z' : [u', v, w'](x', y, z') \rightarrow [u', v, -w'](x', y, -z'). \tag{2.10}$$

This implies that for any solution $\boldsymbol{u}'(\boldsymbol{x}')$, $(S_y \boldsymbol{u}')(\boldsymbol{x}')$ and $(S_z' \boldsymbol{u}')(\boldsymbol{x}')$ are also solutions. In particular, any oblique stripe forming an angle θ with the streamwise direction is associated with its symmetric counterpart, an oblique stripe with an angle $-\theta$. This
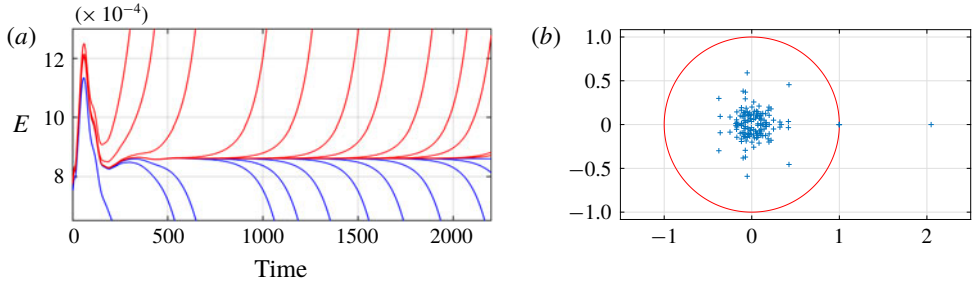
FIGURE 3. (*a*) Edge tracking in a domain tilted by $\theta = 35°$ at $Re = 720$. Trajectories in blue relaminarise directly whereas trajectories in red become turbulent. (*b*) Eigenspectrum for the converged lower-branch TW (LBTW) solution with $\theta = 35°$, $Re = 720$, $L_x = 3.33$ and $L_z = 40$, computed using the Arnoldi algorithm with time horizon $T = 60$. Only one multiplier lies outside the unit circle.

degeneracy is eliminated when computing in a tilted domain with $\theta \neq 0°$ and $\theta \neq 90°$, yet it is useful to keep in mind that all the solutions listed come in pairs.

Another symmetry (linked to the tilted geometry) is the shift-and-reflect symmetry with shifts in the x-direction.

$$S_{rx} : [u, v, w] \left(x + \frac{L_x}{2}, y, z \right) \rightarrow [u, -v, w](x, -y, z). \quad (2.11)$$

This symmetry, specific to each value of L_x, has not been imposed in any of the computations, but it turns out to be verified by all TW solutions found.

3. Parametric study

3.1. *Edge tracking*

The first attempt to identify a simple edge state dynamics is for $Re = 720$, $\theta = 35°$, $L_x = 10$ and $L_z = 40$. These values of L_x and L_z are similar to those in Tuckerman *et al.* (2014), whereas $\theta = 35°$ is well within the experimental and numerical range. The initial condition consists of a random three-dimensional divergence-free velocity field. As shown in figure 3(*a*), the energy $E(t)$ settles to a constant value, the signature of a TW – which can be converged easily using the Newton–Krylov algorithm (Duguet, Willis & Kerswell 2008). The solution travels with a phase velocity c with non-zero streamwise and spanwise components $c_{x'} = 0.77 = 1.15U_b$ and $c_{z'} = 0.06$ in units of U_{cl}, where $U_b = 2/3 * U_{cl}$ is a bulk velocity. The TW propagates with a streamwise phase velocity slightly larger than the flow rate: fluid enters the wave from upstream and is released downstream of it as well as on the sides. The property that lower-branch solutions travel faster than the base flow appears generic to all wall-bounded shear flows. By virtue of the S_z symmetry, a twin TW solution also exists in a domain tilted with angle $-\theta$ with opposite spanwise propagation velocity.

The initial bisections were carried out for $L_x = 10$. The numerical domain with these parameters accommodates three identical wavelengths, and the TWs found do possess this 3-fold periodicity in x. This suggests that a similar TW solution should exist as an edge state in a numerical domain with $L_x \leftarrow L_x/3$ and correspondingly $N_x \leftarrow N_x/3$. This is indeed the case for $L_x = 3.33$. From here on, unless otherwise stated, the value of L_x is set to 3.33. The new TW identified possesses the S_{rx} symmetry specific to
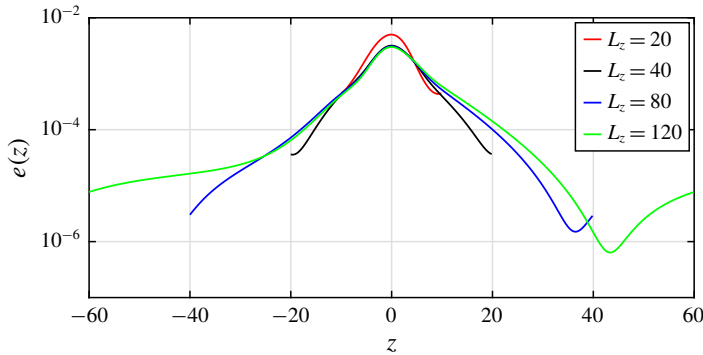
FIGURE 4. Perturbation kinetic energy $e(z)$ for LBTWs with increasing $L_z = 20$, 40, 80 and 120 (logscale). $L_x = 3.33$, $\theta = 35°$, $Re = 720$.

the new value of L_x (compatible with the different symmetry identified for $L_x = 10$). We do not exclude possible subharmonic instabilities for larger values of L_x.

It was determined using the Arnoldi algorithm that the TW solution is linearly unstable but possesses only one real unstable eigenvalue, as expected for edge states. This corresponds to one unstable Floquet multiplier outside the unit circle in figure 3(*b*). The same property also holds for $L_x = 6.66$, 10 and 13.33.

3.2. *Spatial localisation*

Similar bisections were repeated for different values of $L_z = 20$, 40, 80 and 120. The numerical resolution was kept identical except in the z-direction in which N_z was kept proportional to L_z. In all cases, a similar-looking TW solution was identified as an edge state and converged successfully using the Newton algorithm. The z-dependence of the perturbation kinetic energy of the four TWs obtained for different L_z is shown in figure 4. All TWs found here are spatially localised. This suggests that the corresponding TW for $L_z \to \infty$ is a solitary state (its energy drops off exponentially). In what follows, the value of L_z is fixed to 40, keeping in mind that most results are independent of L_z provided L_z is large enough.

3.3. *Self-sustenance and large-scale flow*

We now display visualisations of the TW solutions for 45° in figures 5 and 6. The *xz*-view of the wall-normal velocity in the midplane (see figure 5) reveals a spatial structure very similar to that of turbulent stripes. The three-dimensional structure (see figure 6) features streamwise vortices which are almost parallel to the streamwise direction. Streamwise vortices are naturally associated with streaks (spanwise modulations of the streamwise velocity). The tails of the streaks outside the core of the stripe are deviated by the large-scale flow near both interfaces (Henningson & Kim 1991; Duguet & Schlatter 2013). Interestingly, the streaks for the LBTWs shown in figure 6(*a*,*b*), do not feature the characteristic sinuous structure of other exact coherent states found in smaller domains and fundamental to Waleffe's self-sustaining process (Waleffe 1998). This process assumes that the streamwise vorticity induced by sinuous streak instabilities compensates for its own viscous decay, and that this loop maintains the exact coherent structures in equilibrium.
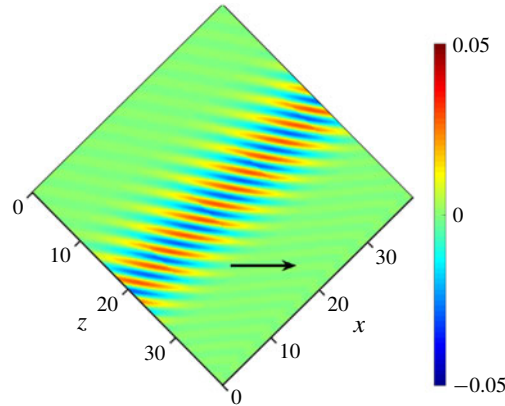
FIGURE 5. LBTW solution computed in a domain tilted by $\theta = 45°$ for $Re = 720$, $L_x = 3.33$ and $L_z = 40$ represented using 12 concatenated copies. Wall-normal velocity field $v(x, y = 0, z)$ (streamwise direction pointing towards positive x and z).
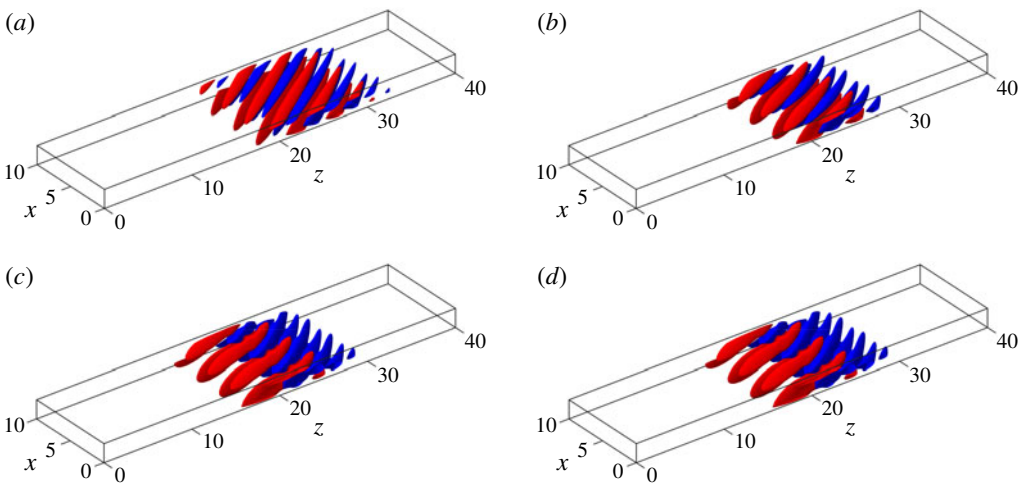

FIGURE 6. (*a*) LBTW solution at $Re = 720$. (*b*) LBTW solution at $Re = 414.25$. (*c*) Upper-branch TW (UBTW) solution at $Re = 414.25$. (*d*) UBTW solution at $Re = 438.74$. Isolevels of streamwise velocity perturbation (red: $u_x = 0.1$, blue: $u_x = -0.1$) for (*a–d*). (*a–d*) Three concatenated copies only.

Here, the streamwise rolls are not sinuous; however, their slight deviation by the large-scale flow contributes to their three-dimensionalisation. This suggests that the nonlinear feedback on the streamwise vorticity, necessary for its sustenance against viscous decay, is operated by the tilting due to the large-scale flow, rather than by the sinuous instability of the streaks. Further work would be necessary to confirm this mechanism. Unlike the LBTW solutions, the UBTW solutions do feature sinuous oscillations of the streaks visible in figure 6(*c,d*).

We investigate now the spatial structure of this large-scale flow. In figure 7(*a*), the planar velocity components are plotted after integration in *y* from wall to wall. As predicted in Duguet & Schlatter (2013), this *y*-integrated velocity field is parallel
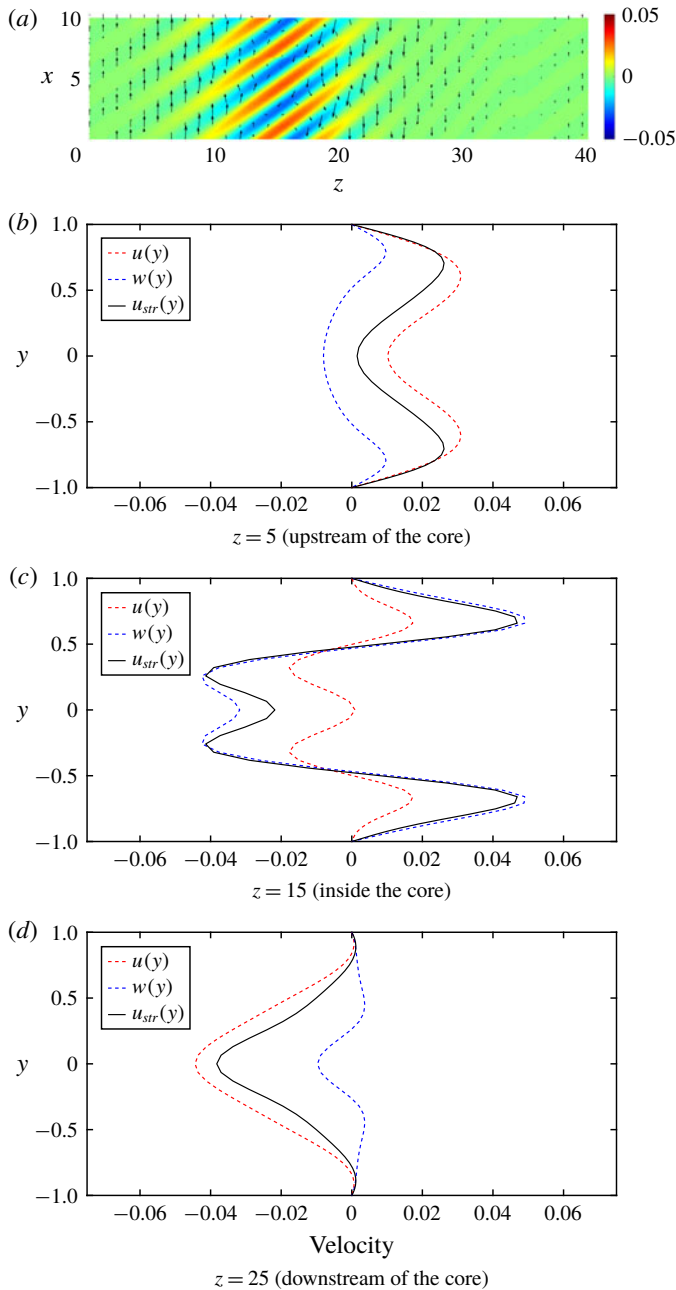
FIGURE 7. Velocity field of LBTW solution at $Re = 720$ at $\theta = 45°$. (*a*) The *xz*-plane with *y*-averaged velocity components as quivers and wall-normal velocity using contours (streamwise direction pointing towards positive *x* and *z*). (*b–d*) The *x*-averaged velocity profiles as functions of *y* for $z = 5$, 15 and 25. These profiles show the large-scale flow around the stripe.

to the interface of the stripe. This observation is fully consistent with the mean flow properties (Barkley & Tuckerman 2007) and with instantaneous visualisations of turbulent stripes (Xiong *et al.* 2015). The simple time-dependence of the TW solution makes the structure of the integrated large-scale flow emerge even without spatial filtering or time-averaging. The non-integrated flow has a strongly three-dimensional structure lost by averaging. The individual components of large-scale flow and their dependence on *y* are plotted in figure 7(*b–d*), after averaging in the short stripe direction *x*, and at different *z* positions outside and inside the active part of the stripe. Robust conclusions emerge independently of the value (positive or negative) of the angle θ. In all cases, the large-scale flow upstream of the stripe has a parallel component pointing downstream, whereas the large-scale flow downstream of the stripe has a parallel component pointing upstream. The large-scale flow outside the active zone differs depending on the side of the stripe considered: the velocity profile upstream is double-humped and stronger near the walls, whereas the velocity profile downstream is single-humped and stronger near the midgap. None of the local velocities exceeds 0.04 (in units of U_{cl}) in absolute value, and such values are attained in the active part of the stripe (here at $z = 15$).

3.4. *Angular dependence*

The same strategy as in § 3.1 was repeated for all values of θ between 0 and 90° in steps of 5°, by fixing $L_x = 3.33$ and $L_z = 40$. The original value of *Re* was chosen again as 720, high enough for turbulent stripes to be observable in numerical simulations. As observed in Barkley & Tuckerman (2007) and Duguet *et al.* (2010), not all angles can support a stable laminar–turbulent interface. Bisection was successful at converging TWs as edge states only for $25° \leqslant \theta \leqslant 60°$. Outside this range, edge tracking proved unfeasible because the turbulent state itself was only short-lived. Continuation of the TWs in *Re* was performed at fixed values of θ, L_x and L_z for the values of θ where TWs were found for $Re = 720$. For each angle, the corresponding TWs emerge in a saddle-node bifurcation at a given value of $Re = Re_{SN}(\theta, L_x, L_z)$ (where Re_{SN} is *Re* at saddle node bifurcation). This is shown in figure 8, where the total kinetic energy *E* is plotted against *Re* for several angles. This figure also contains information on the linear stability of the waves (analysed later). Continuation along the upper branch was stopped as soon as resolution issues started to manifest themselves, a commonly reported issue for upper-branch solutions of shear flows (Waleffe 2001). The smallest value of Re_{SN} is apparently obtained for $\theta = 45°$. Figure 9 displays similar curves for the streamwise and spanwise phase velocities, plotted versus *Re*. Here, the LBTWs are characterised by the larger phase velocities. All TW solutions were found to obey the S_{rx} symmetry for all imposed angles.

Continuation is next carried out in the angle parameter θ for fixed *Re*. This turns out to be a more efficient way to explore the limits of the range of angles where TWs are found. Such data are shown in figure 10 in a effort to highlight the three-dimensional structure of the diagram shown in figures 8 and 9. As shown in figure 10, the range of angles shrinks to the sole value of 45°, whereas it monotonically widens for increasing *Re*. For $Re = 720$, the largest value of *Re* explored in this study, possible angles range from 20° to almost 70°, slightly wider than the range of values of θ accessible by bisection at the same *Re*. It is instructive to plot the value of $Re_{SN}(\theta)$ versus θ for fixed L_x and L_z (cf. figure 12). The curve appears as a slightly asymmetric parabola centred around 45°. This curve bounds the region of existence of the TW solutions in parameter space. As *Re* is gradually increased from zero, the first TW encountered has $\theta = 45°$. As *Re* continues to increase, the range of possible angles widens.
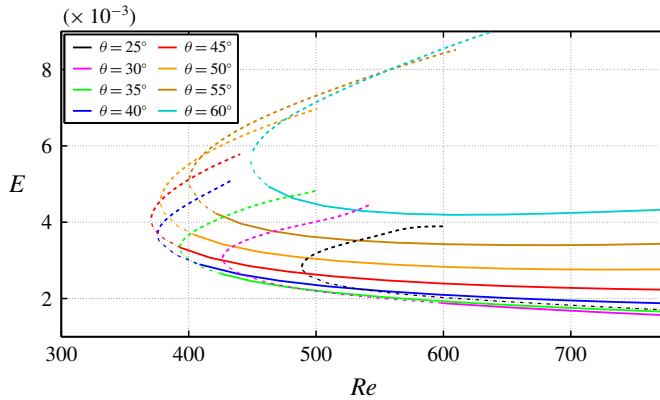
FIGURE 8. Energy for TW solutions versus Re in a domain for different angles θ, $L_x = 3.33$ and $L_z = 40$. Solid lines: TWs with one unstable eigenvalue only (edge states); thin dotted lines: LBTWs with strictly more than one unstable eigenvalue; thick dotted lines: UBTWs.
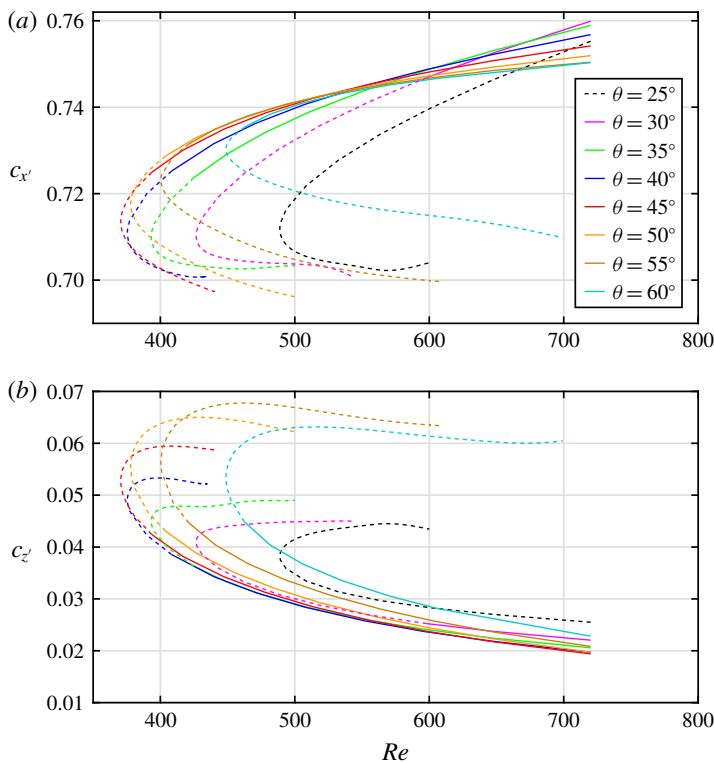

FIGURE 9. Phase velocities for TW solutions in a domain tilted by θ with $L_x = 3.33$ and $L_z = 40$. (*a*) Streamwise component, $c_{x'}(Re)$. (*b*) Spanwise component $c_{z'}(Re)$.

The width of the localised stripe along z can be evaluated by choosing an arbitrary criterion $e_v(z) \geqslant 10^{-4}$. It corresponds to the length of the streaks as visualised in figure 5. The width across the streamwise direction, i.e. along x', was determined
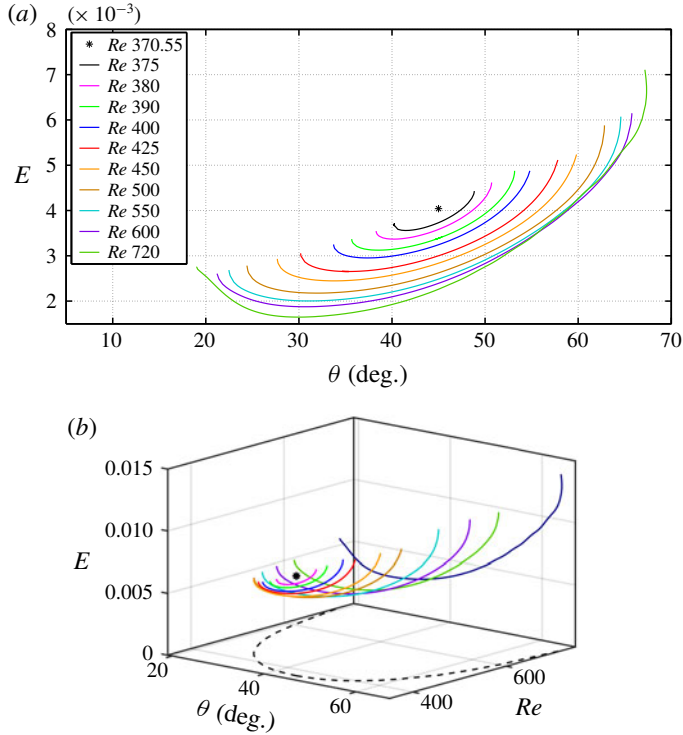
FIGURE 10. Continuation of the TWs in angle for different values of *Re*. (*a*) The (θ, E) projection. (*b*) Three-dimensional projection (θ, Re, E).

from the previous criterion using trigonometric rules. As suggested in figure 4, these quantities are independent of the value of the parameter L_z once it is large enough. For a constant value of *Re*, the width increases almost linearly with θ, see figure 11. The maximum amplitude of these waves, however, is lowest around 45° as is shown in figure 11 using z-profiles of e_v. No clear reason for this property has been identified yet.

3.5. *Hopf bifurcations*

As can be seen in figure 8, the stability of each TW family parametrised by θ changes with *Re* along its respective lower branch. A similar scenario emerges for all values of θ. As *Re* is decreased, starting from $Re = 720$, the LBTW initially possesses one unstable eigenvalue only and is an edge state of the corresponding system. At a given value of $Re = Re_H(\theta, L_x, L_z)$ (where Re_H is *Re* at Hopf bifurcation), two additional complex conjugate eigenvalues become unstable, so that between Re_H and $Re_{SN} < Re_H$ the TW is no longer an edge state.

For each set of parameters, a Hopf bifurcation at $Re = Re_H$ leads to a new branch of RPOs of period T, initially unstable close to Re_H. The loci of these Hopf bifurcation points are shown in figure 12 together with the saddle-node points. In fact, other bifurcations of TWs occur in the interval (Re_{SN}, Re_H), as is clear from the number of unstable eigenvalues at Re_{SN} listed in table 1, which always exceeds three. For instance, for $\theta = 45°$, $L_x = 3.33$ and $L_z = 40$, the primary Hopf bifurcation
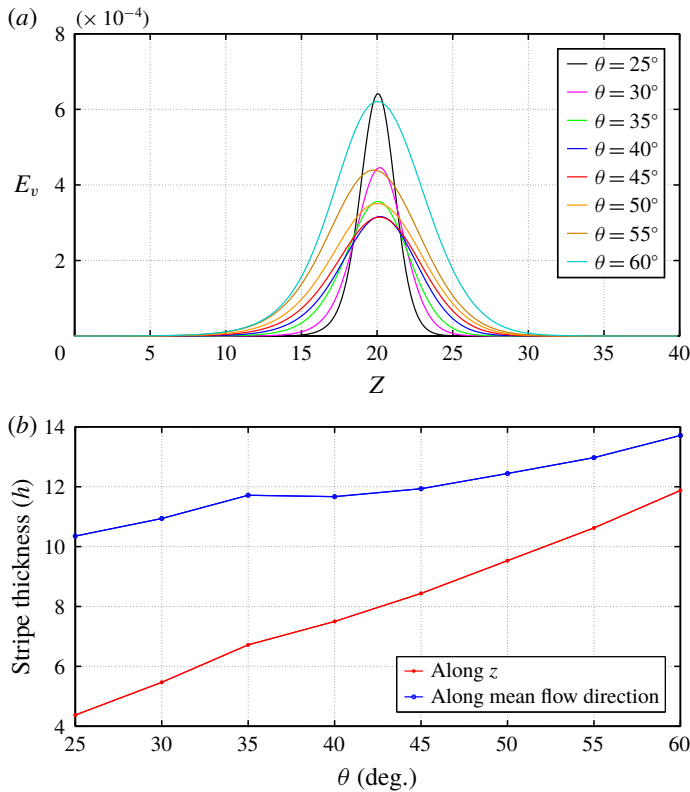
FIGURE 11. (a) Profile of $e_v(z)$ for various tilt angles, $L_x = 3.33$, $L_x = 40$, $Re = 720$, lower-branch solutions. (b) Stripe width versus θ for $Re = 720$, both along the streamwise direction (blue) and across the stripe (red).

(for descending Re) occurs at $Re_H \approx 393$, while the saddle-node bifurcation lies at $Re_{SN} = 370.55$. This Hopf bifurcation breaks the S_{rx} symmetry. The resulting branch of RPOs has been tracked by continuation. One snapshot is displayed in figure 13 using three concatenated copies. Another Hopf bifurcation arises near $Re = 390$. We have not investigated the possible additional bifurcations along the upper branch and/or for other angles and domain sizes. The Hopf bifurcation points $(\theta, Re_H(\theta))$ get increasingly far from the saddle-node points as θ decreases. The values for the period of the RPOs at their respective bifurcation points are reported for most angles in tables 1 and 2.

Unlike the LBTW solutions, the RPO features sinuous oscillations of the streaks. In a frame moving with the original TW velocity, the RPO displays global time-periodic oscillations visible only in the core of the corresponding TW. In this moving frame, they travel upstream, as attested by the space–time diagram in figure 14. The emergence of finite-amplitude time-periodic oscillations propagating on top of a spatially localised TW is strongly reminiscent of the concept of nonlinear global mode put forward in spatially inhomogeneous media (Pier & Huerre 1996). In this picture, the period of the global oscillations is determined at the location where local stability analysis predicts transition from convective to absolute instability. The role of the slowly spatially evolving base flow is played here by the localised TW solutions,
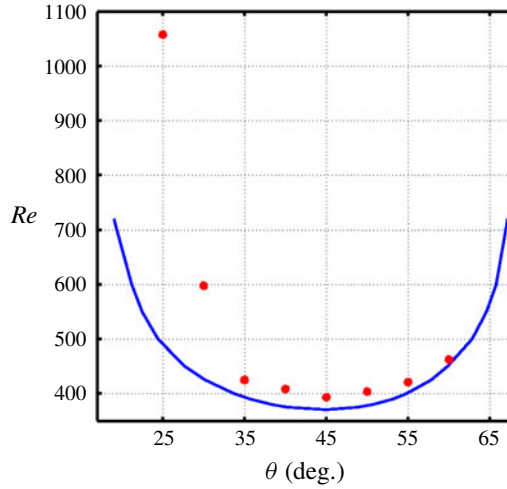
FIGURE 12. Location of saddle-node bifurcations in a (θ, Re) representation ($Re_{SN}(\theta)$, blue solid line), and Hopf bifurcation points ($Re_H(\theta)$, red dots) below which the TWs are no longer edge states.

θ (deg.)	Re_{SN}	Re_H	No. of real (r) and complex (c) unstable eigenvalues on the lower branch in the vicinity of the saddle node point
25	488.8826	1058.12	$1r + 1 \times 2c$
30	426.5995	598.034	$1r + 2 \times 2c$
35	393.2030	424.92	$1r + 2 \times 2c$
40	375.4929	408.44	$1r + 2 \times 2c$
45	370.5567	393.58	$1r + 2 \times 2c$
50	377.8913	403.83	$1r + 2 \times 2c$
55	400.4196	421.16	$1r + 2 \times 2c$
60	448.8425	462.49	$1r + 1 \times 2c$

TABLE 1. Values of Re at the saddle-node bifurcation point Re_{SN} and at the Hopf bifurcation point Re_H of TW solutions for different tilt angles θ and for $L_x = 3.33$ and $L_z = 40$. For $Re > Re_H$ the LBTWs are edge states. Also listed is the stability at the saddle-node point with number of unstable eigenvalues and also the Hopf bifurcation point for LBTW solution branches. See text for definitions.

for which local stability analysis is known to predict absolute instability in the core but stability in the more laminar zones.

3.6. *Minimum Reynolds number*

A recurrent interrogation in earlier investigations of invariant solutions is the minimal value of Re supporting such equilibrium solutions. For instance, Wall & Nagata (2016) have lately reported a non-tilted TW solution existing down to $Re = 665$. This minimisation task can appear endless here given the many parameters present. However, we shortcut this limitation by recalling that (i) the new TW solutions become independent of L_z for L_z large enough, and (ii) the minimal Re corresponds
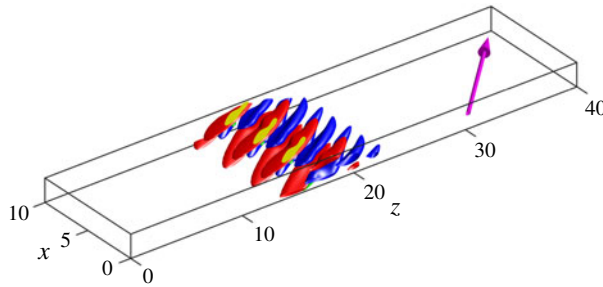
FIGURE 13. Snapshot of an RPO solution computed in a domain tilted by $\theta = 45°$ for $Re = 407$, $L_x = 3.33$ and $L_z = 40$, three concatenated copies. Isolevels of streamwise velocity perturbation (red $u_x = +0.13$, blue: $u_x = -0.13$) and streamwise vorticity (yellow: $\omega_x = 1.0$, green: $\omega_x = -1.0$).

θ	T_{p_1}	T_{p_2}
25	42.4874	N/A
30	29.8828	66.832
35	73.0069	31.548
40	84.3443	29.3557
45	27.6013	96.8748
50	109.1105	25.9726
55	120.2174	23.125
60	127.2664	N/A

TABLE 2. Time period T_{p_1} (respectively T_{p_2}) of the first (respectively second, if any) RPO bifurcating from the LBTW branch for various tilt angles (deduced from the eigenvalues at their respective Hopf bifurcation). The period T_{p_1} is computed at $Re = Re_H$.

to $\theta = 45°$. As a consequence, we define here, pragmatically, the globally minimal Reynolds number as $Re_m = \min_{L_x} Re_{SN}(\theta = 45°, L_x, L_z = 40)$. Hence, Re_m can be determined by fixing $\theta = 45°$, $L_z = 40$ and performing continuation in Re for several values of L_x only. In figure 15, Re_m is displayed as a function of L_x. A local minimum for Re_m is found around 367 and occurs for $L_x = 3.2$. Note that this value is close to the value of 3.33 used here. We do not exclude the possibility for other local minima corresponding to other yet unreported families of TW solutions.

4. Discussions and outlook

We have presented new families of nonlinear TW solutions of channel flow featuring spatial localisation, oblique orientation with respect to the mean flow direction, streamwise vortices and streaks. All the solutions reported here are linearly unstable, although the number of unstable directions is generally very low, ranging from one for edge states up to six for upper-branch solutions near their onset. These solutions are the ones appearing at the lowest value of Re reported so far in channel flow. Interestingly, they do not emerge via a homoclinic snaking scenario as is the case for many non-tilted localised states (Schneider, Gibson & Burke 2010; Knobloch 2015). A few Hopf bifurcations of these new waves occur along the lower branch,
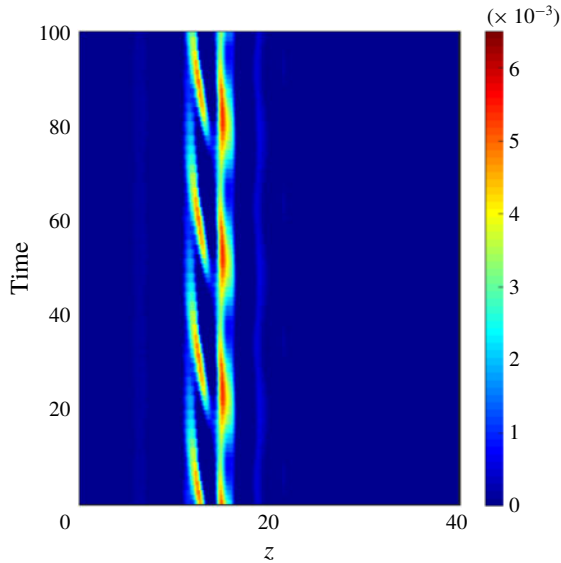
FIGURE 14. Space–time diagram $e_v(z, t)$ for the RPO solution shown in figure 13 over three time periods, $Re = 407$. Frame moving with the original LBTW phase velocity computed for the same value of Re.
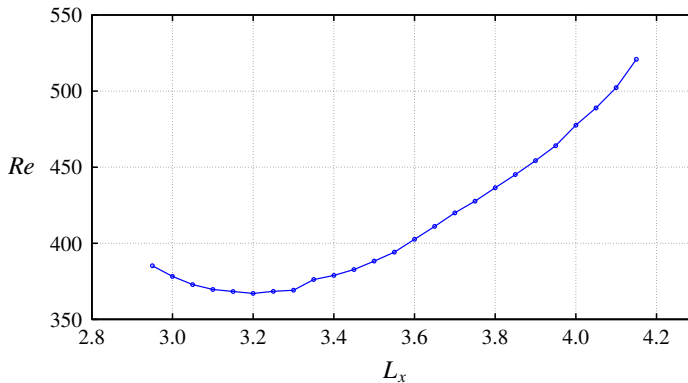

FIGURE 15. Minimum Re versus L_x for $\theta = 45°$ and $L_z = 40$.

rather than the upper branch as commonly reported in shear flows (as in e.g. Zammert & Eckhardt (2015)). The occurrence of such Hopf bifurcations means that for $Re_{SN} < Re < Re_H$ the TWs are no longer edge states and cannot be identified using edge tracking. The success of the method used here hence relies on starting at a sufficiently high value of Re.

This dynamical systems approach to complex stripe patterns can also be applied to other systems displaying spatiotemporal intermittency. The application of edge tracking in tilted domains of plane Couette flow has so far yielded only chaotic edge states rather than exact solutions, even with central symmetry imposed. While this highlights some limitations of the current method, other ways of constructing exact localised solutions are possible, as shown in Gibson & Brand (2014) for plane

Poiseuille flow using spatial windowing or using asymptotic analysis (Deguchi & Hall 2015) in plane Couette flow. We also note a recent cheaper alternative to edge tracking using feedback control (Willis *et al.* 2017) likely to work successfully in our case. More recently, similar families of oblique localised solutions of plane Couette flow have also been constructed by exploiting the possible subharmonic instabilities of formerly known non-localised states (Reetz, Kreilos & Schneider 2019; Reetz & Schneider 2020). This is another promising alternative to edge tracking, although it requires good preliminary knowledge of some solutions. An extension of these ideas to other geometries is encouraged.

For the last two decades, the main motivation to detect and study unstable nonlinear states comes from the conjecture that they constitute a state-space skeleton for the turbulent dynamics (Hof *et al.* 2004; Eckhardt *et al.* 2007; Kawahara *et al.* 2012). TW states, like those reported here, are the simplest instances of such states compatible with the symmetries of the system. The different Hopf bifurcations of these waves lead to new branches of unstable periodic orbits whose further bifurcations, both local and global, are expected to cover the turbulent attractor specific to each tilted domain (Avila *et al.* 2013; Zammert & Eckhardt 2015). This approach is now generally accepted for small constrained systems Budanur *et al.* (2017). However, it remains daring to extend it to spatiotemporal complex situations, such as turbulent stripes, where additional spatial degrees of freedom come into play. Further bifurcations of these modulated waves are expected to give rise to a regime of temporal chaos, which is dynamically consistent with the turbulent behaviour reported – in both constrained and unconstrained numerical domains – at comparable values of *Re* (Tuckerman *et al.* 2014).

At the lowest *Re* typical of figure 1, the experimental transition process involves solitary finite-length bands fully localised in one direction and growing (or receding) in another direction. These bands feature an active head and a passive rear (see e.g. Kanazawa (2018), chap. 5 and Xiao & Song (2020) or figure 2). While growth occurs at the active head, at slightly larger *Re*, stripes extend to lateral boundaries and do not necessarily have a well-defined head. This suggests that the core of the stripe is autonomous and self-sustained. The solutions presented here are localised only in one direction and have unambiguous similarities with the core of the turbulent stripes.

Such an analogy between TWs and turbulence is supported by the agreement between the spanwise wavelength and the streamwise extent of the streaks. More originally, a large-scale flow parallel to the band direction is common to both turbulent stripes and the present TWs. It has been suggested as a crucial player for the spatial proliferation of turbulence in planar flows and as a mechanism to justify the obliqueness of the laminar–turbulent interfaces (Duguet & Schlatter (2013)). This large-scale flow property is specific to localised turbulence. It cannot be interpreted theoretically using the previously found non-localised states, and this justifies the present search for oblique solutions localised in one direction only. *A posteriori*, we have verified that the large-scale flow induces a spanwise propagation velocity explaining the motion of the streaks within the band itself (cf. figure 9). From the investigation of the exact solutions, it was also suggested that the large-scale flow plays a role in the regeneration of the streamwise vorticity inside the band core. Such a possibility had not been considered so far for localised turbulent dynamics, which highlights the utility of exact solutions. As far as the understanding of the energy production mechanisms at the head is concerned, however, other channel solutions with an additional direction of localisation need to be envisioned (Zammert & Eckhardt 2014; Kanazawa 2018).

At slightly higher *Re*, the multitude of possible angles displayed by turbulent stripe patterns falls within the range of angle values where the TWs and their bifurcated states exist. A natural question that arises is whether the range of angles of the TWs bears a direct relation to the selection process of stripe angles in turbulent flows. The critical curve $\theta(Re)$ displayed in figure 12 is at first sight reminiscent of the selection mechanism in other systems with one spatial degree of freedom, such as Rayleigh–Bénard convection (Cross & Hohenberg 1993). However, the nonlinear nature of the wave solutions makes the selection mechanism entirely different. As a consequence of nonlinearity, adding different such solutions together to create new solutions is not allowed. A consequence is that different routes to chaos for different values of θ coexist. On the other hand, the TW with $45°$ is the one persisting down to the lowest *Re*. This is reminiscent of the observation that, close to their onset in *Re* where they are observed, the angle of turbulent stripes saturates at $45°$ (Tao *et al.* 2018; Paranjape 2019). It remains to be understood why no turbulent stripe forms or sustains with an angle larger than $45°$ in realistic domains, whereas this is allowed for TW solutions. This apparent discrepancy is likely to be related to the choice of the tilted domains rather than to the TWs themselves. Indeed, in the comparable tilted domains of plane Couette flow, turbulence is also reported for angles higher than $45°$ (Barkley & Tuckerman 2007), whereas it is not the case in large periodic domains (Duguet *et al.* 2010). This might be related to the issue of stability (in the broad sense) of a given laminar–turbulent interface.

Acknowledgements

Declaration of interests

The authors report no conflict of interest.

REFERENCES

ALAVYOON, F., HENNINGSON, D. S. & ALFREDSSON, P. H. 1986 Turbulent spots in plane Poiseuille flow–flow visualization. *Phys. Fluids* **29** (4), 1328–1331.

AVILA, M., MELLIBOVSKY, F., ROLAND, N. & HOF, B. 2013 Streamwise-localized solutions at the onset of turbulence in pipe flow. *Phys. Rev. Lett.* **110** (22), 224502.

BARKLEY, D. & TUCKERMAN, L. S. 2005 Computational study of turbulent laminar patterns in Couette flow. *Phys. Rev. Lett.* **94** (1), 014502.

BARKLEY, D. & TUCKERMAN, L. S. 2007 Mean flow of turbulent–laminar patterns in plane Couette flow. *J. Fluid Mech.* **576**, 109–137.

BUDANUR, N. B., SHORT, K. Y., FARAZMAND, M., WILLIS, A. P. & CVITANOVIĆ, P. 2017 Relative periodic orbits form the backbone of turbulent pipe flow. *J. Fluid Mech.* **833**, 274–301.

CARLSON, D. R., WIDNALL, S. E. & PEETERS, M. F. 1982 A flow-visualization study of transition in plane Poiseuille flow. *J. Fluid Mech.* **121**, 487–505.

COLES, D. 1965 Transition in circular Couette flow. *J. Fluid Mech.* **21** (3), 385–425.

CROS, A. & LE GAL, P. 2002 Spatiotemporal intermittency in the torsional Couette flow between a rotating and a stationary disk. *Phys. Fluids* **14** (11), 3755–3765.

CROSS, M. C. & HOHENBERG, P. C. 1993 Pattern formation outside of equilibrium. *Rev. Mod. Phys.* **65** (3), 851–1112.

DEGUCHI, K. & HALL, P. 2015 Asymptotic descriptions of oblique coherent structures in shear flows. *J. Fluid Mech.* **782**, 356–367.

DUGUET, Y. & SCHLATTER, P. 2013 Oblique laminar–turbulent interfaces in plane shear flows. *Phys. Rev. Lett.* **110** (3), 034502.

DUGUET, Y., SCHLATTER, P. & HENNINGSON, D. S. 2009 Localized edge states in plane Couette flow. *Phys. Fluids* **21** (11), 111701.

DUGUET, Y., SCHLATTER, P. & HENNINGSON, D. S. 2010 Formation of turbulent patterns near the onset of transition in plane Couette flow. *J. Fluid Mech.* **650**, 119–129.

DUGUET, Y., WILLIS, A. P. & KERSWELL, R. R. 2008 Transition in pipe flow: the saddle structure on the boundary of turbulence. *J. Fluid Mech.* **613**, 255–274.

ECKHARDT, B., SCHNEIDER, T. M., HOF, B. & WESTERWEEL, J. 2007 Turbulence transition in pipe flow. *Annu. Rev. Fluid Mech.* **39**, 447–468.

EHRENSTEIN, U. & KOCH, W. 1991 Three-dimensional wavelike equilibrium states in plane Poiseuille flow. *J. Fluid Mech.* **228**, 111–148.

FAISST, H. & ECKHARDT, B. 2003 Traveling waves in pipe flow. *Phys. Rev. Lett.* **91** (22), 224502.

FUKUDOME, K. & IIDA, O. 2012 Large-scale flow structure in turbulent Poiseuille flows at low-Reynolds numbers. *J. Fluid Sci. Technol.* **7** (1), 181–195.

GIBSON, J. F. 2014 Channelflow: a spectral Navier–Stokes simulator in C++. *Tech. Rep.* University of New Hampshire. Available at Channelflow.org.

GIBSON, J. F. & BRAND, E. 2014 Spanwise-localized solutions of planar shear flows. *J. Fluid Mech.* **745**, 25–61.

GIBSON, J. F., HALCROW, J. & CVITANOVIĆ, P. 2009 Equilibrium and travelling-wave solutions of plane Couette flow. *J. Fluid Mech.* **638**, 243–266.

HAMILTON, J. M., KIM, J. & WALEFFE, F. 1995 Regeneration mechanisms of near-wall turbulence structures. *J. Fluid Mech.* **287**, 317–348.

HASHIMOTO, S., HASOBE, A., TSUKAHARA, T., KAWAGUCHI, Y. & KAWAMURA, H. 2009 An experimental study on turbulent-stripe structure in transitional channel flow. In *Proceedings of the 6th International Symposium on Turbulence Heat and Mass Transfer*. Begel House Inc.

HENNINGSON, D. S. & KIM, J. 1991 On turbulent spots in plane Poiseuille flow. *J. Fluid Mech.* **228**, 183–205.

HOF, B., VAN DOORNE, C. W. H., WESTERWEEL, J., NIEUWSTADT, F. T. M., FAISST, H., ECKHARDT, B., WEDIN, H., KERSWELL, R. R. & WALEFFE, F. 2004 Experimental observation of nonlinear traveling waves in turbulent pipe flow. *Science* **305** (5690), 1594–1598.

ISHIDA, T., DUGUET, Y. & TSUKAHARA, T. 2016 Transitional structures in annular Poiseuille flow depending on radius ratio. *J. Fluid Mech.* **794**, R2.

ISHIDA, T., DUGUET, Y. & TSUKAHARA, T. 2017 Turbulent bifurcations in intermittent shear flows: from puffs to oblique stripes. *Phys. Rev. Fluids* **2** (7), 073902.

JIMÉNEZ, J., KAWAHARA, G., SIMENS, M. P., NAGATA, M. & SHIBA, M. 2005 Characterization of near-wall turbulence in terms of equilibrium and bursting solutions. *Phys. Fluids* **17** (1), 015105.

JIMÉNEZ, J. & MOIN, P. 1991 The minimal flow unit in near-wall turbulence. *J. Fluid Mech.* **225**, 213–240.

KANAZAWA, T. 2018 Lifetime and growing process of localized turbulence in plane channel flow. PhD thesis, Osaka University.

KAWAHARA, G., UHLMANN, M. & VAN VEEN, L. 2012 The significance of simple invariant solutions in turbulent flows. *Annu. Rev. Fluid Mech.* **44**, 203–225.

KLINGMANN, B. 1992 On transition due to three-dimensional disturbances in plane Poiseuille flow. *J. Fluid Mech.* **240**, 167–195.

KNOBLOCH, E. 2015 Spatial localization in dissipative systems. *Annu. Rev. Condens. Matter Phys.* **6** (1), 325–359.

KUNII, K., ISHIDA, T., DUGUET, Y. & TSUKAHARA, T. 2019 Laminar–turbulent coexistence in annular Couette flow. *J. Fluid Mech.* **879**, 579–603.

LEMOULT, G., AIDER, J. L. & WESFREID, J. E. 2013 Turbulent spots in a channel: large-scale flow and self-sustainability. *J. Fluid Mech.* **731**, R4.

NAGATA, M. 1990 Three-dimensional finite-amplitude solutions in plane Couette flow: bifurcation from infinity. *J. Fluid Mech.* **217**, 519–527.

NAGATA, M. & DEGUCHI, K. 2013 Mirror-symmetric exact coherent states in plane Poiseuille flow. *J. Fluid Mech.* **735**.

NEELAVARA, S. A., DUGUET, Y. & LUSSEYRAN, F. 2017 State space analysis of minimal channel flow. *Fluid Dyn. Res.* **49** (3), 035511.

NISHIOKA, M. & ASAI, M. 1985 Some observations of the subcritical transition in plane Poiseuille flow. *J. Fluid Mech.* **150**, 441–450.

ORSZAG, S. A. 1971 Accurate solution of the Orr–Sommerfeld stability equation. *J. Fluid Mech.* **50** (4), 689–703.

PARANJAPE, C. 2019 Onset of turbulence in plane Poiseuille flow. PhD thesis, IST Austria.

PARK, J. S. & GRAHAM, M. D. 2015 Exact coherent states and connections to turbulent dynamics in minimal channel flow. *J. Fluid Mech.* **782**, 430–454.

PIER, B. & HUERRE, P. 1996 Fully nonlinear global modes in spatially developing media. *Physica* D **97**, 206–222.

PRIGENT, A., GRÉGOIRE, G., CHATÉ, H., DAUCHOT, O. & VAN SAARLOOS, W. 2002 Large-scale finite-wavelength modulation within turbulent shear flows. *Phys. Rev. Lett.* **89** (1), 014501.

REETZ, F., KREILOS, T. & SCHNEIDER, T. M. 2019 Exact invariant solution reveals the origin of self-organized oblique turbulent–laminar stripes. *Nat. Commun.* **10** (1), 2277.

REETZ, F. & SCHNEIDER, T. M. 2020 Periodic orbits exhibit oblique stripe patterns in plane Couette flow. arXiv:1912.09889.

SCHNEIDER, T. M., ECKHARDT, B. & YORKE, J. A. 2007 Turbulence transition and the edge of chaos in pipe flow. *Phys. Rev. Lett.* **99** (3), 034502.

SCHNEIDER, T. M., GIBSON, J. F. & BURKE, J. 2010 Snakes and ladders: localized solutions of plane Couette flow. *Phys. Rev. Lett.* **104** (10), 104501.

SEKI, D. & MATSUBARA, M. 2012 Experimental investigation of relaminarizing and transitional channel flows. *Phys. Fluids* **24** (12), 124102.

SKUFCA, J. D., YORKE, J. A. & ECKHARDT, B. 2006 Edge of chaos in a parallel shear flow. *Phys. Rev. Lett.* **96** (17), 174101.

STUART, J. T. 1960 On the non-linear mechanics of wave disturbances in stable and unstable parallel flows. Part 1. The basic behaviour in plane Poiseuille flow. *J. Fluid Mech.* **9** (3), 353–370.

TAO, J. J., ECKHARDT, B. & XIONG, X. M. 2018 Extended localized structures and the onset of turbulence in channel flow. *Phys. Rev. Fluids* **3** (1), 011902.

TSUKAHARA, T. & ISHIDA, T. 2015 Lower bound of subcritical transition in plane Poiseuille flow. *Nagare* **34**, 383–386.

TSUKAHARA, T., SEKI, Y., KAWAMURA, H. & TOCHIO, D. 2005 Dns of turbulent channel flow at very low Reynolds numbers. In *4th International Symposium on Turbulence and Shear Flow Phenomena*. Begel House Inc.

TUCKERMAN, L. S., CHANTRY, M. & BARKLEY, D. 2019 Patterns in wall-bounded shear flows. *Annu. Rev. Fluid Mech.* **52**, 343–367.

TUCKERMAN, L. S., KREILOS, T., SCHROBSDORFF, H., SCHNEIDER, T. M. & GIBSON, J. F. 2014 Turbulent–laminar patterns in plane Poiseuille flow. *Phys. Fluids* **26** (11), 114103.

VISWANATH, D. 2007 Recurrent motions within plane Couette turbulence. *J. Fluid Mech.* **580**, 339–358.

WALEFFE, F. 1998 Three-dimensional coherent states in plane shear flows. *Phys. Rev. Lett.* **81** (19), 4140.

WALEFFE, F. 2001 Exact coherent structures in channel flow. *J. Fluid Mech.* **435**, 93–102.

WALL, D. P. & NAGATA, M. 2016 Exact coherent states in channel flow. *J. Fluid Mech.* **788**, 444–468.

WEDIN, H. & KERSWELL, R. R. 2004 Exact coherent structures in pipe flow: travelling wave solutions. *J. Fluid Mech.* **508**, 333–371.

WILLIS, A. P., DUGUET, Y., OMEL'CHENKO, O. & WOLFRUM, M. 2017 Surfing the edge: using feedback control to find nonlinear solutions. *J. Fluid Mech.* **831**, 579–591.

XIAO, X. & SONG, B. 2020 The growth mechanism of turbulent bands in channel flow at low Reynolds numbers. *J. Fluid Mech.* **883**, R1.

XIONG, X., TAO, J., CHEN, S. & BRANDT, L. 2015 Turbulent bands in plane-Poiseuille flow at moderate Reynolds numbers. *Phys. Fluids* **27** (4), 041702.

ZAMMERT, S. & ECKHARDT, B. 2014 Streamwise and doubly-localised periodic orbits in plane Poiseuille flow. *J. Fluid Mech.* **761**, 348–359.

ZAMMERT, S. & ECKHARDT, B. 2015 Crisis bifurcations in plane Poiseuille flow. *Phys. Rev.* E **91** (4), 041003.